Article

Modeling of a Quasi-Resonant DC Link Inverter Dedicated to Common-Mode Voltage and Ground Current Reduction

Marek Turzyński [1],* and Michal Frivaldsky [2]

[1] Faculty of Electrical and Control Engineering, Gdańsk University of Technology, 80-233 Gdańsk, Poland

[2] Department of Mechatronics and Electronics, Faculty of Electrical Engineering and Information Technologies, University of Žilina, 010 26 Žilina, Slovakia; michal.frivaldsky@feit.uniza.sk

* Correspondence: marek.turzynski@pg.edu.pl

Abstract: In this paper, the modeling methodology of the AC drive system with a Parallel Quasi-Resonant DC Link Inverter (PQRDCLI) is described. A presented modeling approach is an attractive tool used for the effective evaluation of a common-mode (CM) voltage and grounds current reduction methods. Designed models of inverter, induction machine (IM), and cable are simple, thus the methods for parameter extraction are not complicated. Verification of the proposed modeling approach was realized with the use of the the Synopsys (Mountain View, CA, USA) SABER simulator, while simulation results were experimentally verified. Operation principles of the proposed PQRDCLI converter topology are also described. Based on simulation and experimental results, it was confirmed that the proposed PQRDCLI solution represents required performance within the reduction of common-mode voltage and ground current in electric drives. Moreover, comparisons from a simulation complexity point of view have been performed to the existing methods. The evaluation is being shown at the end of the paper. It is confirmed that the presented method is simple, fast, accurate, and robust as well.

Keywords: quasi-resonant DC link inverter; common-mode voltage; AC drive; circuit simulation; modeling; voltage gradient; ground leakage current

1. Introduction

The use of the modern power semiconductor devices enables the operation of variable-frequency drives with carrier frequencies up to 200 kHz [1]. However, an increase of switching frequency results in EMI (Electromagnetic Interference Emissions) problems appearance; thus, the level of generated conducted EMI disturbances is one of the main evaluation criteria of AC drive inverters. High frequency EMI disturbances are propagated by magnetically and capacitively coupled parasitic circuits [2,3]. It should be noted that common-mode (CM) voltage at motor terminals is partially transferred through capacitive coupling to a non-grounded motor shaft, which results in shaft voltage appearance [4,5]. As a consequence, the probability of occurrence of destructive electrostatic discharge machining (EDM) bearing currents increases according to the growth of CM voltage amplitude [6]. EDM currents are the result of a breakdown of insulating lubricating grease films in rotating bearings. This is caused by overshoot the maximum breadown value of the machine shaft voltage. As a result of the EDM current's influence, pits, craters, or stripes appear on rolling surfaces of machine bearings, which leads to faster degradation of bearings. Finally, bearings are destroyed and electric drive becomes out of order. This problem grows accordingly to the dissemination of electric drives fed by inverters, what shall be reflected also within the drive system reliability. Some reduction methods of bearing

currents occurrence are proposed, for example the use of conductive greases, application of insulated bearings or motor shaft grounding. However, these methods do not fully eliminate the bearing's currents problem, because these solutions do not affect the CM voltage. Possible elimination of the discussed problem can be realized through the use of hybrid bearings with ceramic rolling elements. The disadvantage of this approach is that the market cost of this solution is very high.

Due to the propagation mechanism, the level of CM disturbances is strictly connected with *dv/dt* value resulting from the transistor's commutation processes. Hence, high *dv/dt* CM voltage slopes generate large peaks of leakage current circulating in a protective ground wire, what reflects in excitation of the circulating bearing currents [7,8]. It is worth mentioning that a large amplitude of leakage currents may cause undesirable operation of residual current circuit-breakers, the wrong activation of fire alarms, or various sensors operation disturbances.

Various methods for reduction of these negative effects are proposed, including installation of filters [5,9] applying modified modulation methods [10] or using modified DC/AC inverters [8,11]. It should be noted that in some cases, the effectiveness of these solutions is questionable. Hence further research is required. Hence, the problem of methods development focused on bearing's currents elimination, and CM voltage influence reduction must be evaluated as still valid.

Modeling and simulation may be a useful tool for the evaluation of CM disturbance reduction methods, which is especially helpful at the early design stage of drive. Considering CM disturbance propagation paths, the models of inverter, cable, and motor should be included within the overall model of AC drive. Proposed solutions, dedicated to EMI analyses, ensures high accuracy of simulation results in a range of frequency up to tens of MHz [12]. These models take into account many aspects, e.g., the impact of parasitic capacitances (including nonlinear capacitances of semiconductors), resistances and inductances of paths and cables, skin effects, etc. [13–15]. However, models become complex, which leads to an increase of the computational time of numerical calculations. As a result, the simulation process is time-consuming, and it often cannot be successfully finished due to numerical problems. This problem is especially distinguishable when more complicated topologies of inverters are simulated, for example, resonant or quasi-resonant inverters or multilevel inverters with an increased number of switches. It should also be noted that most of the proposed models dedicated to EMI analysis require complicated methods of parameter extraction, e.g., based on Wheeler/Schneider formulas [16], finite-element calculations [17], or PEEC (Partial Element Equivalent Circuit) methods [18]. Therefore, a trade-off between model complexity, availability of parameters, and accuracy is the main criterion of model usability.

Effective CM voltage level reduction and limitation of ground currents peak values may be achieved by using Parallel Quasi-Resonant DC Link Inverter (PQRDCLI) [8,19]. Simulation enables evaluation of PQRDCLI properties at the beginning of the designing process when a target topology is developed. However, this task requires to use the models of semiconductor devices reflecting the dynamics of their switching process. Moreover, the impact of parasitic components such as resistances and inductances of paths and cables or capacitive couplings cannot be omitted.

In this paper, a modeling approach of AC drive fed by PQRDCLI is presented. Compared to other existing solutions, the models of the inverter, cable, and induction motor are not complicated, and their parameters are easy to extract. Presented approach enables realizing the simulation of the overall AC drive system with satisfactory accuracy. Simulated results were compared with measured ones to confirm the accuracy of the proposed models. Models presented in this paper were developed and validated using the SABER simulator; however, the proposed solution may be adapted without significant modifications to other circuit simulators, e.g., PSpice, LTSpice, etc. The presented modeling approach may be successfully used for the evaluation of reduction of CM voltage and i_{PE} current.

2. Model of AC drive with PQRDCLI

2.1. Model of PQRDCLI in Saber Simulator

If Parallel Quasi-Resonant DC-Link Inverters (PQRDCLI) are considered, the oscillations in a quasi-resonant circuit are excited once per commutation of inverter switches. Hence, voltage pulse-time modulation methods, including Space Vector Pulse Width Modulation (SVPWM), may be effectively adapted to PQRDCLI. A scheme of considered PQRDCLI is presented in Figure 1 [8]. During the first part of the resonant cycle, inverter input voltage v_F is reduced to zero, enabling switching of inverter transistors T_{F1}–T_{F6} under Zero Voltage Conditions (ZVS). After the transition of the inverter vector to the new state, voltage v_F is rebuilt to the supply voltage V_{DC}. By controlling inverter input voltage gradients dv_F/dt during the resonant process, inverter output voltages gradients dv/dt are limited, what enables the reduction of overvoltage spikes. Due to the use of two transistors T_1, T_2 included in the DC link circuit, a full separation of induction motor from supply source V_{DC} may be realized. It results in reduction of CM voltage levels during inverter zero voltage state. Thus, compared to hard-switched inverter (considered to be conventional three-phase, two-level bridge inverter) probability of EDM currents occurrence of motor bearings fed by proposed PQRDCLI is significantly reduced. Moreover, the reduction of CM voltage dv/dt gradients leads to attenuation of ground leakage current pulses and mitigation of circulating bearing currents.
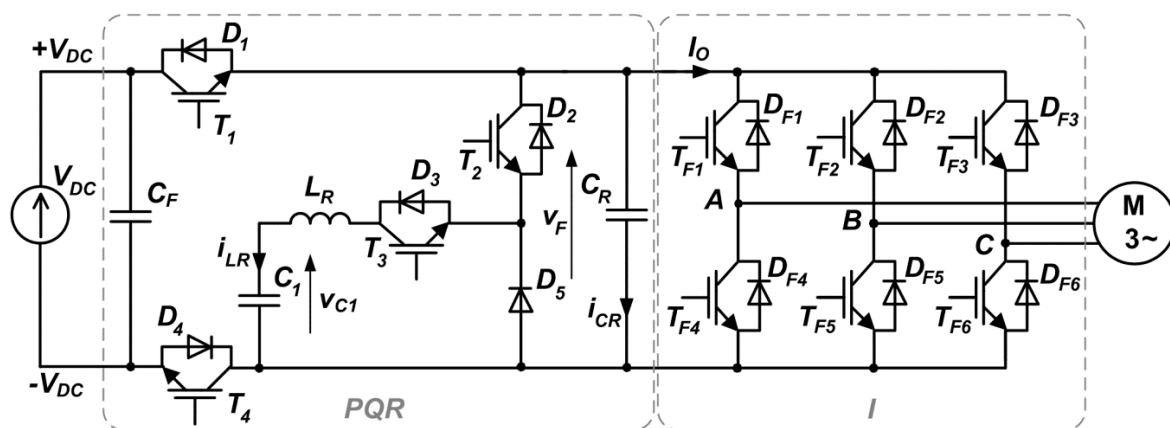

Figure 1. Parallel quasi-resonant DC link inverter: PQR—parallel quasi-resonant circuit, I—inverter, M—induction motor.

Operational waveforms of PQRDCLI are presented in Figure 2. Voltage v_{C1} (across the capacitor C_1) is assumed to be constant during all operational cycles. For time intervals $t < t_0$ or $t < t_7$ the inverter operates at steady state. Transistors T_1 and T_2 are turned on, while the resonant circuit is inactive. Load current I_O flows through transistors T_1, T_2, and voltage v_F is equal to V_{DS}. The resonant process is initiated by switching on transistor T_2 under Zero Current Conditions (ZCS) at the moment t_0. Resonant Inductor current i_{LR} starts to increase linearly within the circuit V_{DC}-T_1-T_2-D_3-L_R-C_1-T_4. This period ends at the moment t_1 when i_{LR} current reaches $I_{LR(max)}$ value, and sufficient energy is accumulated in a resonant inductor L_R to ensure discharging of resonant capacitor C_R. It should be noted that transistor T_3 should be switched-off during period <t_0, t_1> if v_F voltage zero states are applied to form a zero voltage vector of the inverter. If the inverter is switched between two active states, transistor T_3 remains turned on during the full resonant cycle.
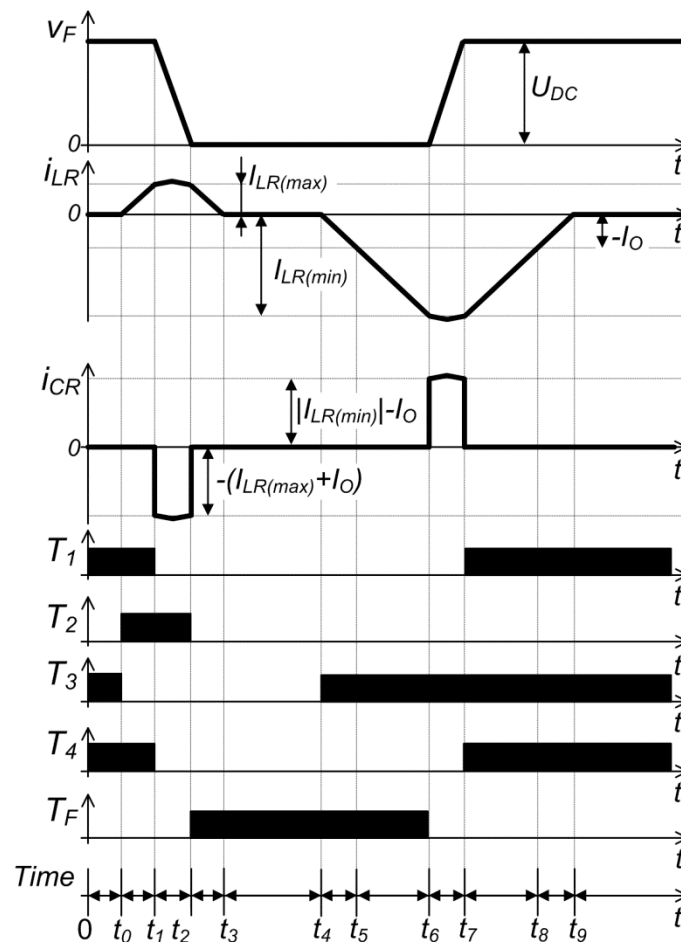
Figure 2. Transient waveforms at positive load current I_O.

At the moment t_1, transistors T_1, T_4 are turned off at ZVS conditions. As a result, a resonant inductor current i_{LR} flows through the circuit L_R-C_1-C_R-T_2-D_3, which forces resonant discharge of resonant capacitor C_R by the current, which is a sum of i_{LR} and I_O currents. During period $<t_1, t_2>$ voltage v_F is reduced to zero, which ensures the turn-on of inverter transistors T_F under ZVS conditions since moment t_2 (signal T_F represents all of the inverter transistors at on- state). Transistor T_2 is turned off under ZVS conditions at the moment t_2, thus resonant inductor current starts to decrease within the circuit L_R-C_1-D_5-D_3. Meanwhile, the load current I_O flows through the short-circuited inverter. At the moment, t_3 current i_{LR} falls to zero. Period $<t_3, t_4>$, when v_F voltage is reduced to zero, it shall be maintained for an arbitrary time interval, which allows forming a zero voltage vector of the inverter. If the inverter is switched between two active states, this period is omitted. At the moment, t_3 transistor T_3 is turned on at ZCS conditions. As a result, the resonant inductor current starts to decrease in the circuit L_R-T_3-D_2-T_F. When current i_{LR} falls to $I_{LR(min)}$ value, inverter transistors are switched to the new active state. Current i_{LR} starts to circulate in the circuit L_R-T_3-D_2-T_F, which forces the charging of capacitor C_R and rebuilding of voltage v_F. It should be noted that i_{CR} current should be positive, hence $|I_{LR(min)}| > I_O$. After rebuilding of v_F voltage to V_{DC} value, during period $<t_6, t_7>$ the excess of energy accumulated in the resonant inductor is returned to the supply source V_{DC} by the current circulating within the circuit L_R-T_3-D_2-T_1/D_1-V_{DC}-T_4/D_4-C_1. At the moment t_7, the resonant inductor current reaches zero, and the resonant cycle ends.

The modulator signal initiates every operation cycle. If signal initialization is considered, the commutation of transistors is delayed due to the start of the resonant cycle. Moment t_2 (Figure 2) is detected by respective comparators at the instant when voltage v_F falls below reference value $v_{F(ref)} = 5$ V. Switching of transistors T_2 and T_F is then possible. The second comparator detects

the moment when voltage v_F is rebuilding into V_{DC} value at the time t_6. It enables the turn-on of transistors T_1, T_4. Adopted PQRDCLI control strategy with the controlled length of resonant periods ensures the stabilization of capacitor C_1 voltage. It enables control of gradient $|dv_F/dt|$ regardless of the amplitude and direction of the load current I_O [8]. However, an estimation of i_{LR} current is required to calculate the length of period $<t_0, t_1>$, when resonant circuit transistors T_1, T_2, T_4 are turned on. Similarly, this applies for determination of the length of period $<t_2, t_5>$, when turning-on T_F transistor short-circuits the inverter.

A simulation model of experimental PQRDCLI is presented in Figure 3. For the model of capacitors C_F, C_1, and C_R, the equivalent schematic with a series connection of capacitance, resistance ESR and inductance ESL is adopted [20]. The model of resonant inductor L_R consists of an inductance connected in series with resistance [21]. Simplified formulas were used to calculate resistances and inductances of main paths and buses in dependency on their geometrical dimensions [22]. This approach does not take into account skin effects, but it enables decreasing the PQRDCLI model complexity and simplifies the procedure of model parameters extraction. Capacitors C_{ip1} and C_{ip2} model a capacitive coupling between DC buses and inverter chassis/heatsink, and their values could be directly measured using an impedance analyzer ($C_{p1} = C_{p2} = 260$ pF).
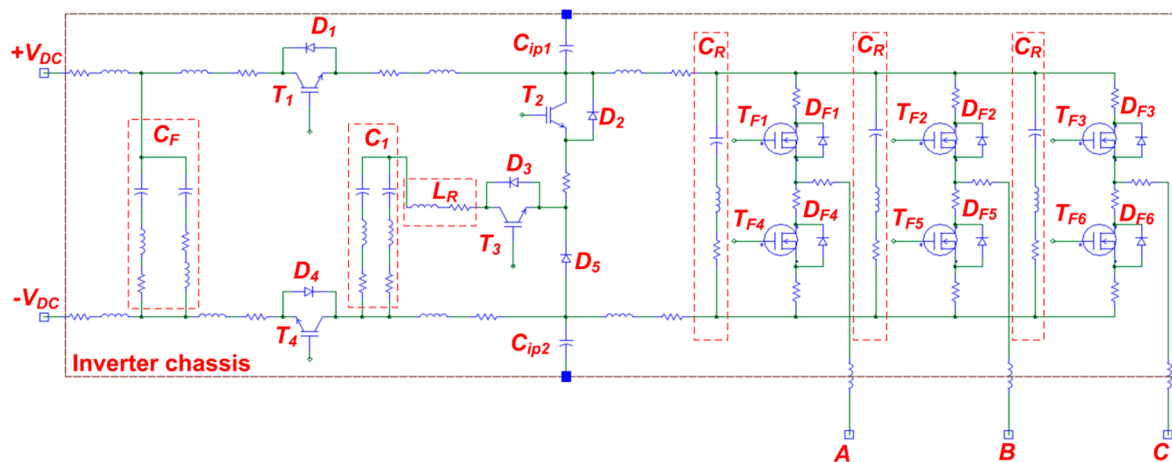

Figure 3. A simulation model of proposed PQRDCLI in SABER@Sketch editing window of SABER simulator.

Models of semiconductor devices should take into account the influence of parasitic nonlinear capacitances and dynamic behavior during switching processes. Within the simulation model of PQRDCLI, behavioral models of of Insulated Gate Bipolar Transistors (IGBTs), and Metal-Oxide Semiconductor Field-Effect Transistors (MOSFETs) are applied based on the modeling approach presented in Ref. [23]. Moreover, the model of the diode, enables simulating a reverse recovery effect during the turn-off process [24]. The model of the control system is realized as a "user block" named "CONTROL PQRDCLI" and programmed using the mixed-technology language for electromechanical design and analysis MAST programming language (Figure 4). Initially, the values of load current I_O before and after the commutation of transistors are estimated in dependency on modulator signals [8]. It refers to the measurement of the actual value of output currents.
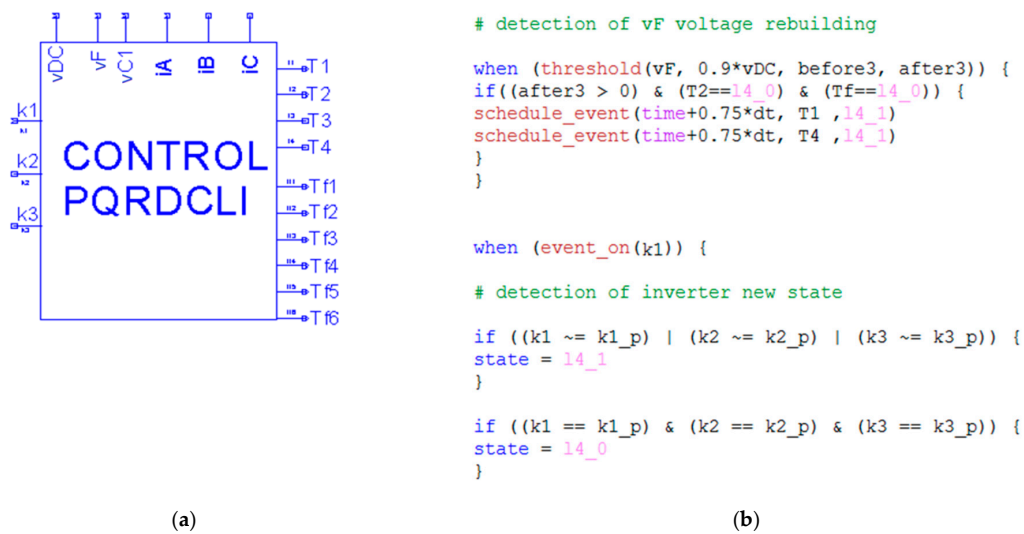
```
# detection of vF voltage rebuilding

when (threshold(vF, 0.9*vDC, before3, after3)) {
if((after3 > 0) & (T2==14_0) & (Tf==14_0)) {
schedule_event(time+0.75*dt, T1 ,14_1)
schedule_event(time+0.75*dt, T4 ,14_1)
}
}


when (event_on(k1)) {

# detection of inverter new state

if ((k1 ~= k1_p) | (k2 ~= k2_p) | (k3 ~= k3_p)) {
state = 14_1
}

if ((k1 == k1_p) & (k2 == k2_p) & (k3 == k3_p)) {
state = 14_0
}
```

(**a**)   (**b**)

Figure 4. Model of the PQRDCLI control system: (**a**) SABER@Sketch symbol; (**b**) exemplary part of code written in MAST programming language.

Consequently, $I_{LR(min)}$ and $I_{LR(max)}$ values are calculated as a function of voltages V_{DC}, v_{C1}, and function of the values of load current I_O and required value of gradient $|dv_F/dt|$. Finally, the length of switching sequences for each transistor is individually calculated. Required current and voltage sensors are adopted from Saber@Sketch parts library. Moreover, models of transistor drivers (defined as "user blocks" written in MAST) reflect gate voltage rise and fall times and gate current level.

2.2. Model of an Induction Motor Common-Mode Impedance

The appearance of CM voltage v_{N-PE} in the electric drive is caused by an inverter operation [25,26]. This voltage applies to a motor CM impedance, which generates a current flow in a protecting wire connecting the inverter and motor. It should be noted that v_{N-PE} acts on a stator winding and capacitive couplings between stator windings and motor frame or shaft and additionally between the shaft and grounded frame [25]. Hence, an equivalent scheme of a motor common-mode impedance may be considered (Figure 5), whose main components are:

v_{CM}—common-mode voltage source,

Z_{SF}—impedance between stator windings and grounded frame,

C_{SR}—capacitance between short-circuited stator windings terminals and motor shaft,

Z_{RF}—impedance between the motor shaft and frame,

S—short-circuited input terminals of star-connected stator windings,

F—motor frame

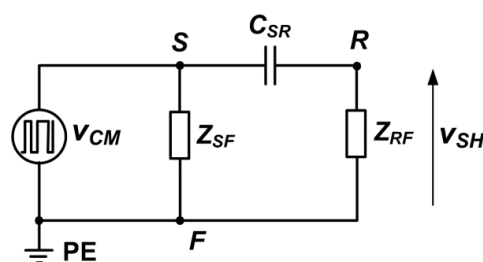R—motor shaft.

v_{SH}—shaft voltage.

Figure 5. A model of an induction machine common-mode impedance.

The model of impedance Z_{RF} between the motor shaft and frame is composed from inherent motor capacitance C_{RF} between shaft and frame and from bearings determined by the type of applied bearings. If standard bearings are used, a model of a single bearing is composed of capacitor C_{BRG} representing capacitance between the inner and outer race of bearing (Figure 6a). Additionally, a switch *SW* is used to model a breakdown of insulating lubricating grease films in a rotating bearing, which results in EDM current appearance [4,9]. If insulated bearings (standard bearings with additional insulation layers) are used, a model of single bearing presented in Figure 6a is modified by adding a capacitor C_{INS}. It represents the capacitance of an insulating layer between the motor frame and the outer race of bearing, as it is presented in Figure 6b [9]. If hybrid bearings with ceramic rolling elements are used, a model of a single bearing is only composed of a capacitor C_{BRG} without switch *SW*. (Figure 6c).
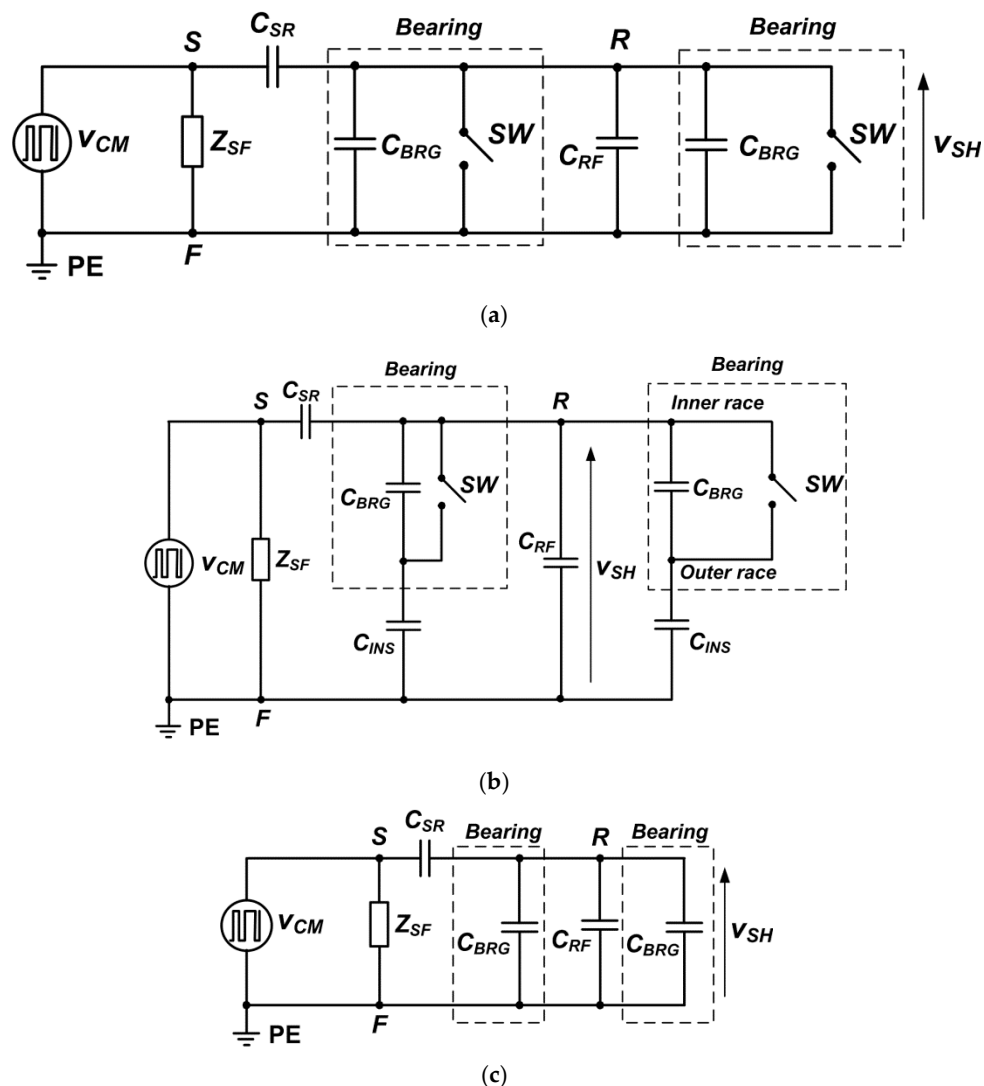

(a)

(b)

(c)

Figure 6. An equivalent scheme of an induction motor common-mode impedance: (**a**) with standard bearings; (**b**) with insulated bearings; (**c**) with hybrid bearings.

As is presented in Figure 7a, IM common-mode impedance is measured between input terminals of stator windings and a motor frame. Moreover, during the measurement, the input terminals of stator windings should be connected. Capacitive couplings distinctly dominate obtained frequency characteristic $Z_{Cm}(\omega)$ with a small impact of inductive components in frequency bands "*b*" and "*d*" (Figure 7b) [15,27]. The typical value of capacitance C_{SR} is small - about 10 pF to 100 pF, hence current i_{PE} circulating through the ground wire is mainly determined by impedance Z_{SF} [28]. However,

bearings are affected by a shaft voltage v_{SH}, which arises from $v_{N\text{-}PE}$ voltage value and parameters of capacitors forming impedance Z_{RF}. Considering previous relations, it is possible to propose a lumped parameter CM impedance model of IM with hybrid bearings (Figure 8).
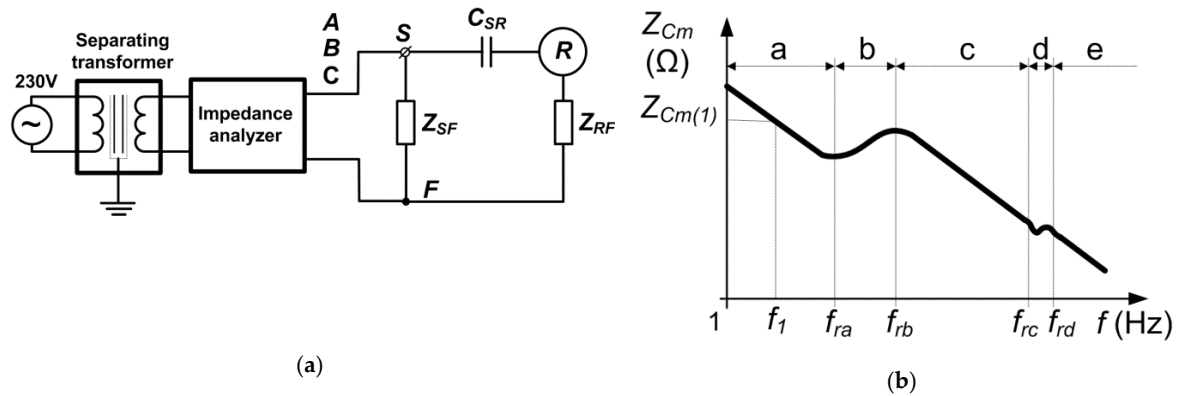

Figure 7. Measurement of IM common-mode impedance Z_{Cm}: (**a**) measurement setup; (**b**) $Z_{Cm}(\omega)$ characteristic.
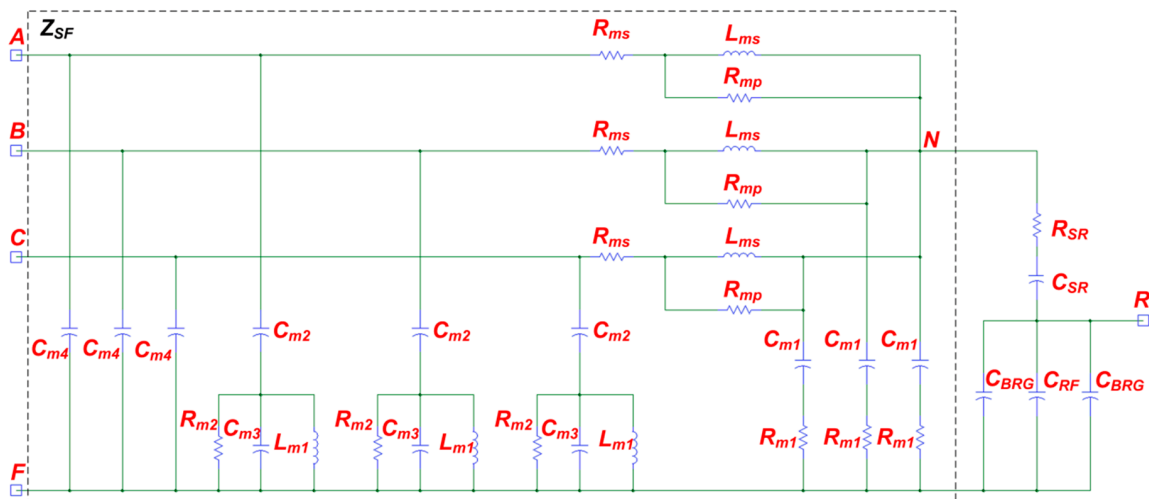

Figure 8. A model of IM common-mode impedance in the editing window of SABER simulator.

Impedance Z_{SF} is modeled by a set of resistances, capacitors, and inductors, whose parameters are extracted from the measured $Z_{Cm}(\omega)$ characteristic. Omitting an influence of capacitance C_{SR}, in frequency band "*e*" (Figure 7b), impedance Z_{Cm} is determined by capacitor C_{m4} together with a series connection of capacitors C_{m2} and C_{m3}:

$$\left| Z_{Cm}(\omega) \right| = \frac{C_{m2} + C_{m3}}{3\omega(C_{m2}C_{m3} + C_{m2}C_{m4} + C_{m2}C_{m4})} \tag{1}$$

Moreover, analogously in section "*c*," it can be assumed that:

$$\left| Z_{Cm}(\omega) \right| = \frac{1}{3\omega(C_{m2} + C_{m4})} \tag{2}$$

In the section "*a*," when frequency $f \ll f_{ra}$, value of impedance Z_{Cm} results from a parallel connection of capacitors C_{m1}, C_{m2}, and C_{m4}:

$$\left| Z_{Cm}(\omega) \right| = \frac{1}{3\omega(C_{m1} + C_{m2} + C_{m4})} \tag{3}$$

At frequency f_{ra}, a series resonance between inductor L_{ms} and capacitor C_{m1} occurs. Hence it can be assumed that the resonant frequency f_{ra} is given by:

$$f_{ra} \approx \frac{1}{2\pi \sqrt{L_{ms}C_{m1}}}. \tag{4}$$

On the boundary between bands "b" and "c," a parallel resonance between inductor L_{ms} and capacitors C_{m2} and C_{m4} are recognized. Similarly, in-band "d" series and parallel resonances between inductors L_{m1} and capacitors C_{m2} and C_{m3} are observed. In bands "a" and "b," absolute value of impedance Z_{Cm} may be described as follows:

$$
\begin{aligned}
&\left| Z_{Cm}(\omega) \right| \\
&= \frac{1}{3} \sqrt{\left(\frac{Z_1(Z_1{}^2 + Z_2{}^2)}{Z_1{}^2 + (\omega(C_{m2}+C_{m4})(Z_1{}^2+Z_2{}^2)-Z_2)^2} \right)^2 + \left(\frac{(Z_2 - \omega(C_{m4}+C_{m2})(Z_1{}^2+Z_2{}^2))(Z_1{}^2+Z_2{}^2)}{Z_1{}^2 + (\omega(C_{m2}+C_{m4})(Z_1{}^2+Z_2{}^2)-Z_2)^2} \right)^2}
\end{aligned}
\tag{5}
$$

where

$$Z_1 = R_{m1} + R_{ms} + \frac{(\omega L_{ms})^2 R_{mp}}{(\omega L_{ms})^2 + R_{mp}{}^2} \tag{6}$$

and

$$Z_2 = \frac{\omega L_{ms} R_{mp}{}^2}{(\omega L_{ms})^2 + R_{mp}{}^2} - \frac{1}{\omega C_{m1}} \tag{7}$$

Similarly, for frequency $f \gg f_{rB}$ in sections "c", "d" and "e", the following formulas are applicable:

$$
\begin{aligned}
&\left| Z_{Cm}(\omega) \right| \\
&= \frac{1}{3} \sqrt{\left(\frac{Z_3(Z_3{}^2 + Z_4{}^2)}{Z_3{}^2 + (\omega C_{m4}(Z_3{}^2+Z_4{}^2)-Z_4)^2} \right)^2 + \left(\frac{(Z_4 - \omega C_{m4}(Z_3{}^2+Z_4{}^2))(Z_3{}^2+Z_4{}^2)}{Z_3{}^2 + (\omega C_{m4}(Z_3{}^2+Z_4{}^2)-Z_4)^2} \right)^2}
\end{aligned}
\tag{8}
$$

where

$$Z_3 = \frac{(\omega L_{m1})^2 R_{m2}}{(\omega L_{m1})^2 + R_{m2}{}^2(\omega^2 L_{m1} C_{m3} - 1)^2} \tag{9}$$

and

$$Z_4 = \frac{\left(1 - \omega^2 L_{m1} C_{m3}\right)\omega L_{m1} R_{m2}{}^2}{(\omega L_{m1})^2 + R_{m2}{}^2(\omega^2 L_{m1} C_{m3} - 1)^2} - \frac{1}{\omega C_{m2}} \tag{10}$$

Model parameters are extracted from the measured CM impedance characteristic (Figure 7b). Firstly, parameters of capacitors C_{m2}, C_{m3}, and C_{m4}, inductor L_{m1}, and resistance R_{m2} may be obtained based on experimental measurement of $Z_{Cm}(\omega)$ characteristic within bands "c," "d" and "e." Calculations are done using Equations (8)–(10) and curve fitting method, e.g., fminsearch function of MathWorks (Natick, MA, USA) MATLAB/GNU Octave programs [29]. Capacitor C_{m1} may be parameterized by applying modified Equation (3):

$$C_{m1} = \frac{1}{6\pi f_1 Z_{Cm(1)}} - C_{m2} - C_{m4} \tag{11}$$

where $Z_{Cm(1)}$ is an absolute value of machine CM impedance at frequency f_1 (Figure 7b). Next, inductor L_{ms} may be identified:

$$L_{ms} = \frac{1}{4\pi^2 f_{ra}{}^2 C_{m1}} \tag{12}$$

A set of equations derived from Equations (5)–(7) has to be solved in order to calculate values of resistances R_{m1} and R_{mp}. In that case, Z_{Cm} values measured for frequencies f_{ra} and f_{rb} should be taken into account as reference values. Values of winding resistances R_{ms} are directly measured using measuring devices (impedance analyzer).

Considering IM with hybrid bearings (Figure 6c), impedance Z_{RF} is determined by capacitances C_{BRG} and C_{RF}. Bearing capacitance C_{BRG} may be directly measured using an LCR meter or impedance analyzer before bearing installation. Then the values of C_{SR} and C_{RF} may be extracted. In the first step, an impedance Z_{Rm} is measured using a test bench presented in Figure 9a.
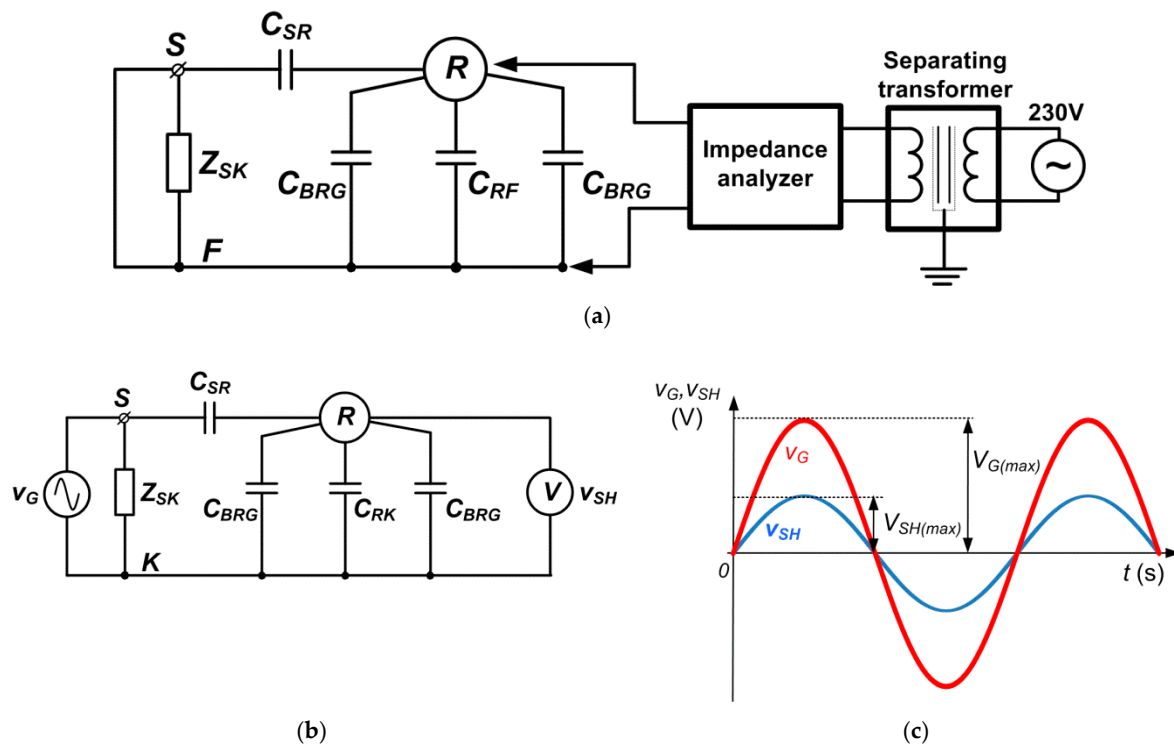

(a)

(b)   (c)

Figure 9. Measurement of C_{SR} and C_{RF}: (**a**) laboratory setup for identification of impedance Z_{Rm} characteristic; (**b**) measurement setup for Bearing Voltage Ratio (*BVR*) evaluation; (**c**) v_G and v_{SH} voltages waveforms.

It should be noted that input terminals of stator windings are short-circuited to the motor frame, hence Z_{Rm} impedance characteristic results from:

$$|Z_{Rm}(\omega)| = \frac{1}{\omega(2C_{BRG} + C_{RF} + C_{SR})} \tag{13}$$

Next, the Bearing Voltage Ratio (*BVR*) [6] defined as:

$$BVR = \frac{C_{SR}}{2C_{BRG} + C_{RF} + C_{SR}} \tag{14}$$

may be gained by introducing a sinusoidal voltage source v_G (e.g., signal generator) between terminals *S* and motor frame *F* and measuring of shaft voltage v_{SH} between the motor shaft and frame (Figure 9b). *BVR* can be calculated as follows:

$$BVR = \frac{V_{G(max)}}{V_{SH(max)}} \tag{15}$$

where $V_{G(max)}$ and $V_{SH(max)}$ are amplitudes of voltages v_G and v_{SH} (Figure 9c), hence, from Equation (14), the capacitance of C_{SR} is given by:

$$C_{SR} = \frac{2C_{BRG} + C_{RF}}{1 - BVR} \tag{16}$$

Moreover, substituting Equation (16) to Equation (13) capacitance of C_{RF} may be obtained:

$$C_{RF} = \frac{1 - BVR}{\omega|Z_{Rm}(\omega)|} - 2C_{BRG}. \tag{17}$$

In the presented model structure (Figure 8), a small resistor ($R_{SR} = 1\ \Omega$) was implemented between node N and capacitor C_{SR} in order to improve the numerical stability of the model. The proposed model of IM CM impedance may also be applied when another type of bearings are used. If insulated bearings are installed (Figure 6b), parameter identification of capacitors C_{SR}, C_{BRG}, C_{RF}, C_{INS} is also possible as it is presented in Ref. [9]. In that case, a measurement procedure requires to ensure sufficient speed of motor shaft (more than 300 rpm) to form a thin insulating lubricating grease film within a bearing body [9]. If standard bearings are applied to motor construction (Figure 6a), individual identification of C_{BRG} and C_{RF} is impossible. However, the presented measurement method for capacitor C_{SR} and impedance Z_{Rm} is still valid if the motor shaft rotates with sufficient speed. A modeling approach of Z_{SF} impedance may be successfully applied regardless of applied bearing types.

In this paper, a model of 7.5 kW IM with hybrid bearings 6308-2RS (ZCS Ceramit) is being considered. Parameters of the motor model are depicted in Table 1.

Table 1. Common-mode impedance model parameters of a 7.5 kW motor with hybrid bearings 6308-2RS (ZCS Ceramit).

Parameter	Value
C_{m1}	1.31 nF
C_{m2}	64 pF
C_{m3}	102 pF
C_{m4}	255 pF
C_{SR}	105 pF
C_{RF}	1310 pF
C_{BRG}	29 pF
L_{m1}	23.9 μH
L_{ms}	7.53 mH
R_{m1}	308 Ω
R_{m2}	2.86k Ω
R_{mp}	5911 Ω
R_{ms}	5.31 Ω
R_{SR}	1 Ω

2.3. Model of Cable

A model of four-wire cable connecting the inverter and motor is presented in Figure 10. The model is composed of resistances R_{cs} connected in series with inductors L_{cs}, mutual inductances M_{cs}, and ground capacitances C_{c1} connected in series with resistor R_{c1}. Terminals A, B, C are connected to the inverter outputs, and terminals A', B', C' is linked to the motor. Common-mode cable impedance characteristic $Z_{Cc}(\omega)$ may be measured within the laboratory setup, as is presented in Figure 11a.
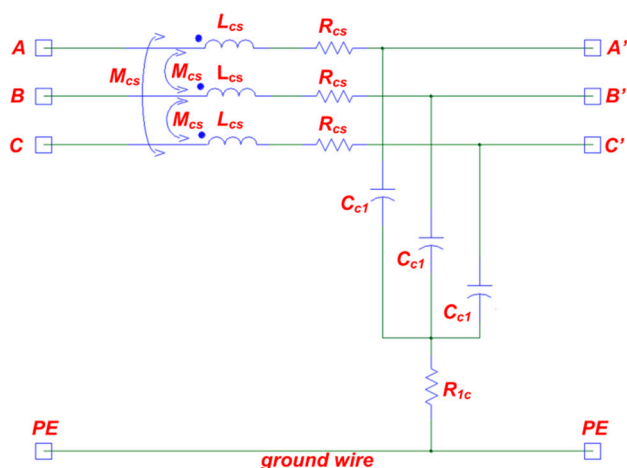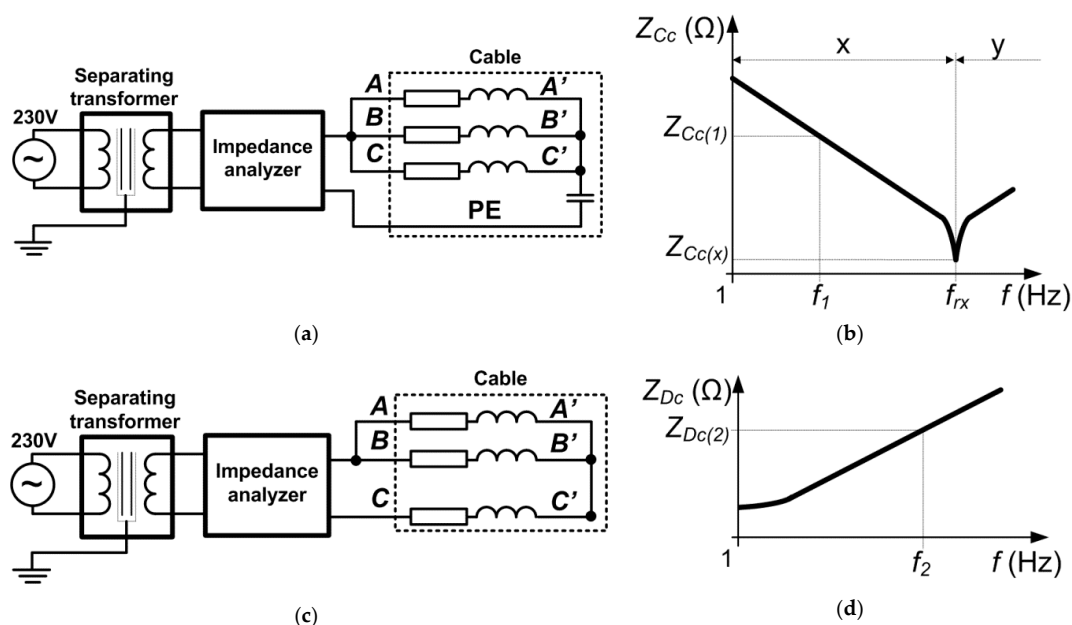
Figure 10. A model of cable.

Figure 11. Measurement of cable model parameters: (**a**) measurement setup for $Z_{Cc}(\omega)$ characteristic; (**b**) $Z_{Cc}(\omega)$ characteristic; (**c**) measurement setup for $Z_{Dc}(\omega)$ characteristic; (**d**) $Z_{Dc}(\omega)$ characteristic.

Based on $Z_{Cc}(\omega)$ characteristic (Figure 11b), one resonant frequency (f_{rx}) is identified at series resonance, which is formed by cable series inductances and C_{c1}. If frequency f is significantly lower than f_{rx} (band "x"), the characteristic of cable CM impedance is dominated by a ground capacitance C_{c1}. Hence, the value of C_{c1} may be extracted as follows:

$$C_{c1} = \frac{1}{6\pi f_1 Z_{Cc(1)}} \tag{18}$$

where $Z_{Cc(1)}$ is an absolute value of cable CM impedance at frequency f_1 (Figure 11b), next, an equivalent inductance L_{Ce} may be obtained:

$$L_{Ce} = \frac{1}{4\pi^2 f_{rx}^2 C_{c1}} \tag{19}$$

Based on $Z_{Dc}(\omega)$ characteristic (Figure 11d), which is obtained by the measurement (Figure 11c), an equivalent differential-mode inductance L_{De} may be calculated:

$$L_{De} = \frac{Z_{Dc(2)}}{2\pi f_2} \tag{20}$$

where $Z_{Dc(2)}$ is an absolute value of cable impedance Z_{Dc} at frequency f_2 (Figure 11d), analyzing schematics presented in Figure 11a, Figure 11c, and considering the proposed cable model structure, the following system of equations may be formulated:

$$\begin{cases} L_{Ce} = L_{cs} + 2M_{cs} \\ L_{De} = (3L_{cs} + M_{cs})/2 \end{cases} \tag{21}$$

Hence, solving a system of Equations (21), values of L_{cs} and M_{cs} are described as follows:

$$L_{cs} = (4L_{De} - L_{Ce})/5 \tag{22}$$

and

$$M_{cs} = (3L_{Ce} - 2L_{De})/5 \tag{23}$$

The value of resistor R_{cs} shall be measured directly using an impedance analyzer or LCR meter. Based on $Z_{Cc}(\omega)$ characteristic (Figure 11b), it may be assumed that:

$$R_{c1} = Z_{Cc(x)} - R_{cs}/3 \tag{24}$$

where $Z_{Cc(x)}$ is a value of Z_{Cc} impedance at resonant frequency f_{rx}.

In this paper, a cable model of 2.5 m length is considered. The model parameters are presented in Table 2.

Table 2. Cable model parameters.

Parameter	Value
C_{c1}	77 pF
L_{cs}	670 nH
M_{cs}	310 nH
R_{cs}	18 mΩ
R_{c1}	2.52 Ω

3. Simulation and Experimental Results

Parameters of experimental PQRDCLI are depicted in Table 3. The Control system with the Vector Sigma-Delta modulator [30] is implemented using the STM32F407 microcontroller operating with the sampling frequency of 20 kHz. To simplify control algorithms and calculations, MOSFETs were used as main inverter transistors T_F. It should be noted that the turn-off process of MOSFET proceeds without tail current observed for IGBT. If IGBT is used, the IGBT turn-off tail current will influence the resonant capacitor current i_{CR}, which would result in significant changes of dv_F/dt values during the period $<t_5, t_6>$. However, IGBTs were applied in the resonant circuit due to better dynamic parameters of anti-parallel diodes and lower conduction losses compared to MOSFETs.

Table 3. PQRDCLI specification.

Parameter	Specification
Rated output power	2 kW
V_{DC}	260 V
T_1–T_4, D–D_5	IGBT-IRG4PC40 (Infineon)
T_F–T_{F6}, D_F–D_{F6}	N-MOSFET FDA50N50 (Fairchild)
C_F, C_1	470 μF (electrolytic) + 220 nF (polypropylene)

Within experimental measurements, the bench power supply unit (EA-PSI 9750-20 3U) provides a stabilized voltage of 260 VDC to fed PQRDCLI. The inverter load was formed by a 7.5 kW induction

motor with hybrid bearings 6308-2RS (ZCS Ceramit, Tłuczań, Poland). Voltage and current waveforms were recorded using the Tektronix (Beaverton, OR, USA) DPO4034 oscilloscope equipped with the high voltage differential probe P5205A (100 MHz) and the current probe TCP2020 (50 MHz). Consequently, the simulation model of proposed PQRDCLI, IM, and cable was built as hierarchical models of Synopsys (Mountain View, CA, USA) Saber@Sketch and were used to model the AC drive system in the configuration, as presented in Figure 12. The star-connected capacitors C_d (3×0.68 nF) were used to measure the common-mode voltage $v_{\text{N-PE}}$ referred to the Protective Earthing (PE) ground potential. V_{DC} supply ground capacitances ($C_{sp1} = C_{sp2} = 72$ nF) were measured using impedance analyzer. Sinusoidal voltage sources V_ω were added to simulate an influence of IM rotational electromotive force.
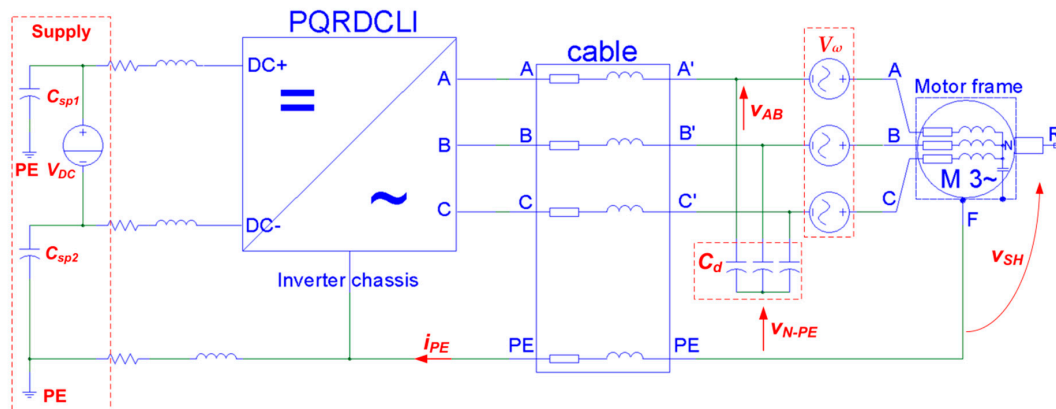
Figure 12. Simulation model of AC drive system with PQRDCLI.

A good coherence between simulated and measured characteristics of CM impedance of motor and cable is depicted in Figure 13. Identified results of measurements confirm resonant frequencies of simulated $Z_{Cm}(\omega)$ and $Z_{Cc}(\omega)$ characteristics. Moreover, values of Z_{Cm} and Z_{Cc} impedances at resonant frequencies are close to measured values. The proposed method of IM CM impedance modeling may be useful within the range of frequency up to 5 MHz. For higher frequencies, an impact of additional capacitive and inductive couplings, which is not considered within the proposed model, is distinguishable. These additional couplings may cause significant differences of impedance characteristics, even between motors of the same type; hence they should be identified for each machine individually [31].
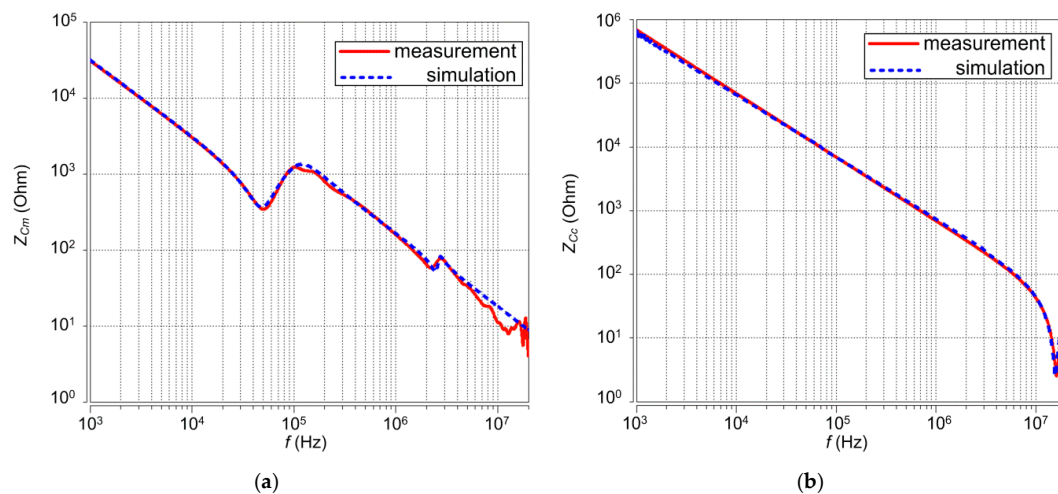

Figure 13. Measured and simulated frequency characteristics of the common-mode impedance: (**a**) induction machine; (**b**) cable.

Evaluation of the PQRDCLI model includes a comparison of characteristic operational waveforms with experimental ones. Good accuracy of waveforms between simulation and measurement of voltage v_F and current i_{LR} is shown in Figure 14. Special focus is given on comparisons of the maximal and minimal values of i_{LR} and on the comparisons of the gradient dv_F/dt during voltage v_F rise and fall periods ($dv_F/dt \approx \pm 200$ V/µs). Attenuated voltage v_F oscillations, which appear after v_F rise/fall to V_{DC} value, are visible for both experimental and simulated waveforms.
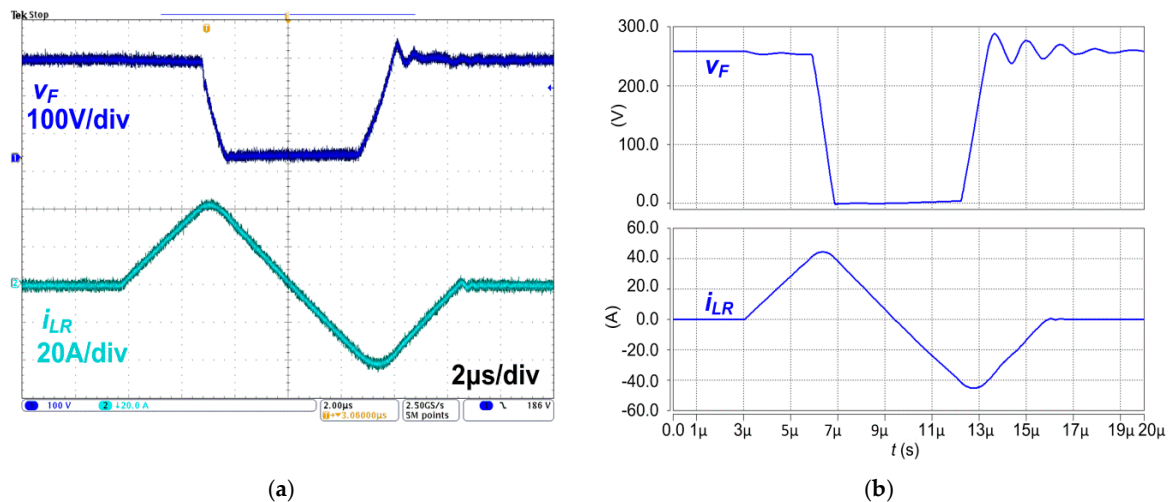
Figure 14. PQRDCLI Quasi-resonant voltage v_F and current i_{LR} waveforms at related output power (2 kW): (**a**) measurement; (**b**) simulation.

The reduction of gradient dv_F/dt enables the limitation of dv/dt values of inverter output voltages. As a result, the overvoltage spikes of the line- to - line voltages acting on motor stator windings do not exceed $1.16 \times V_{DC}$ (without using any additional filters or snubbers). This statement is confirmed by simulation and measurement as well (Figure 15).
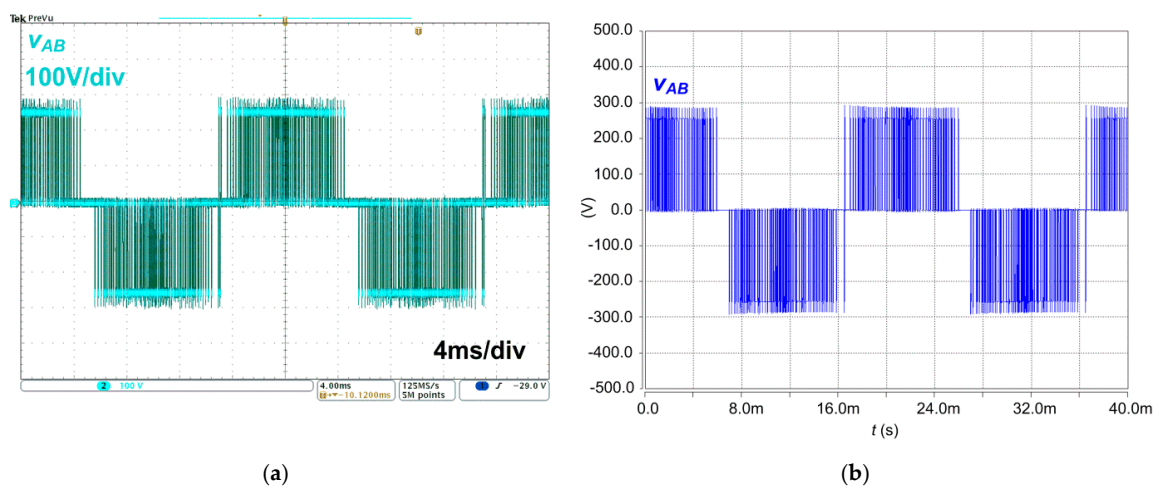

Figure 15. Line -to-line voltage v_{AB}: (**a**) measurement; (**b**) simulation.

A satisfied accuracy is recorded for simulated waveforms of common-mode voltage $v_{N\text{-}PE}$, shaft voltage v_{SH}, and ground current i_{PE} (Figure 16). In conventional two-level hard- switched inverter, $v_{N\text{-}PE}$ levels are equal $\pm V_{DC}/6$ for active vectors and $\pm V_{DC}/2$ for zero vectors. If PQRDCLI is being used, levels of $v_{N\text{-}PE}$ are limited to $\pm V_{DC}/6$ due to CM voltage reduction for zero vectors [8]. However, as a result of the interaction between motor ground capacitances and parasitic nonlinear capacitances of transistors T_1, T_2, $v_{N\text{-}PE}$ is not fully reduced to zero during the inverter zero vector.

Hence, a bias shift (about 25 V) is observed for both measured and simulated $v_{N\text{-}PE}$ waveforms. Shaft voltage v_{SH} reflects the envelope of $v_{N\text{-}PE}$ voltage with $BVR \approx 5\%$, which is a typical value for off-the-shelf motors [32]. Due to the reduction of CM voltage, levels of shaft voltage v_{SH} are also limited, decreasing the possibility of EDM bearing's current occurrence. Compared to $dv_{N\text{-}PE}/dt$, shaft voltage gradients dv_{SH}/dt are slightly decreased, resulting from the influence of stator windings—motor frame impedance of IM. The waveform of ground leakage current i_{PE} is determined by $dv_{N\text{-}PE}/dt$ values and CM impedance of propagation path between induction machine and inverter. Simulated i_{PE} current waveform with peak values close to 500 mA is coherent with measured one, proving correctness of adopted modeling approach.
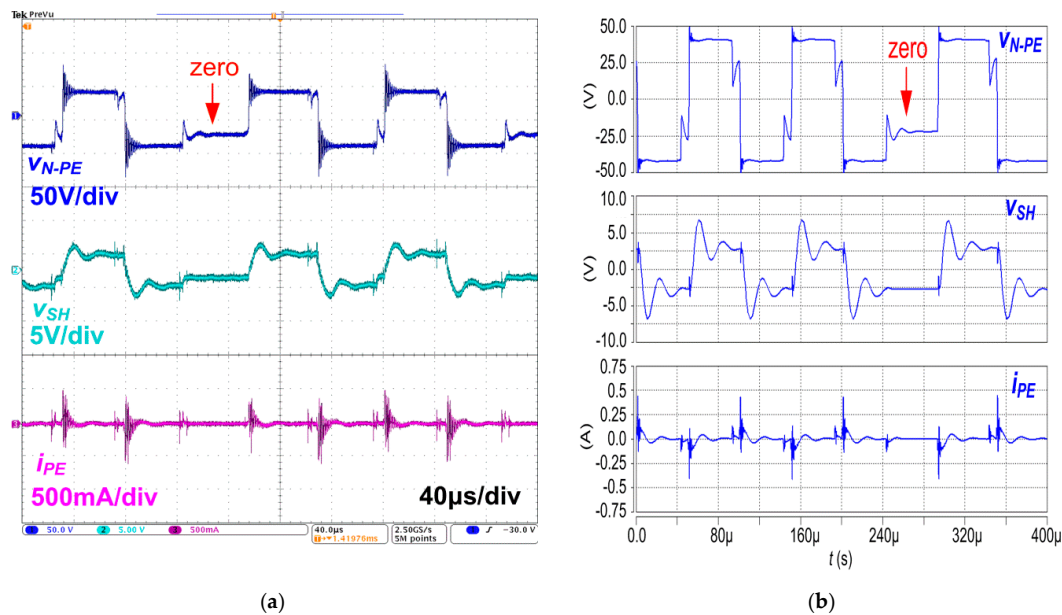

Figure 16. Waveforms of CM voltage $u_{N\text{-}PE}$, shaft voltage u_{SH}, and leakage ground current i_{PE} (**a**) measurement; (**b**) simulation.

A satisfying agreement between experimental and simulated spectra of voltage $v_{N\text{-}PE}$ and current i_{PE} is obtained (Figure 17). Simulated spectra levels and most significant resonant frequencies are recognized in experimental results, especially for frequency range lower than 1 MHz. Nevertheless, $v_{N\text{-}PE}$ spectrum peak at f = 1MHz is not as clear as it is observed for measured results. For frequency range lower than 1 MHz, coherence between simulated and measured CM voltage spectra is satisfactory. Comparing simulated and measured spectra of current i_{PE}, the peak observed at a frequency around 1MHz is recognized for both cases. However, for the simulated spectrum, this peak is shifted about 0.3 MHz relative to the results of the measurement. A significant peak around 3 MHz is noted in the measured i_{PE} spectrum, but it is not observed for the results of the simulation. It should be noted that an influence of omitted components and phenomena (e.g., skin effects, more detailed modeling of capacitive ground couplings) should be taken into account to increase the accuracy of simulated spectra in a range of frequency higher than 1 MHz. Nevertheless, the complexity of models will increase sifgnificantly.
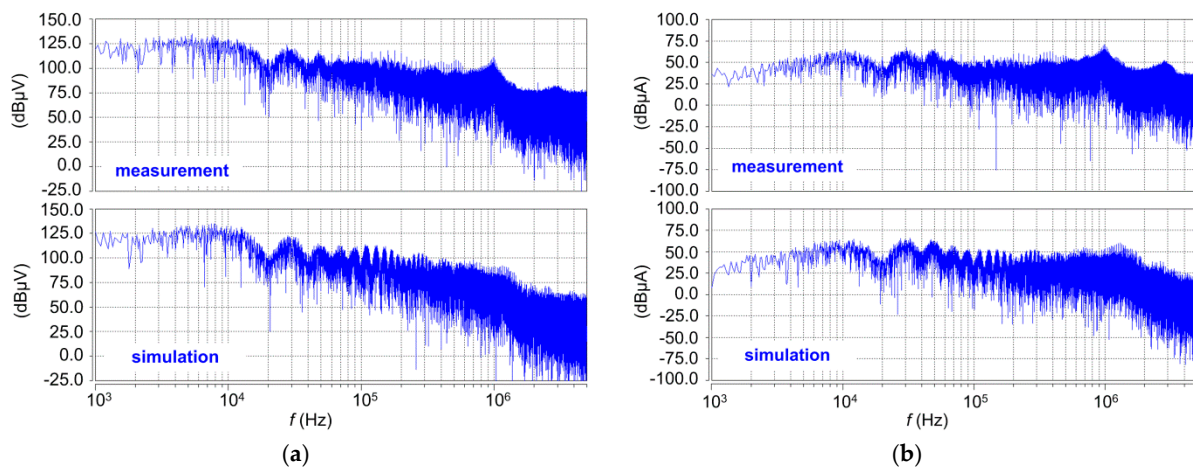
Figure 17. Simulated and measured spectra: (**a**) voltage $v_{\text{N-PE}}$; (**b**) current i_{PE}.

The described modeling approach was used to model a system with a hard-switched inverter (considered to be general three-phase, two-level bridge inverter, whose main parameters are the same as reported for PQRDCLI). Such a drive system may be treated as a system without common-mode voltage reduction. The obtained results of simulation have been validated by comparison with the results of experimental measurement. In this case, a good correlation between simulated and measured results was recorded. Characteristic levels (at steady states) of CM voltage are distinguishable for active inverter vectors, when $v_{\text{N-PE}} = \pm V_{DC}/6$ and for zero vectors, when $v_{\text{N-PE}} = \pm V_{DC}/2$ (Figure 18).
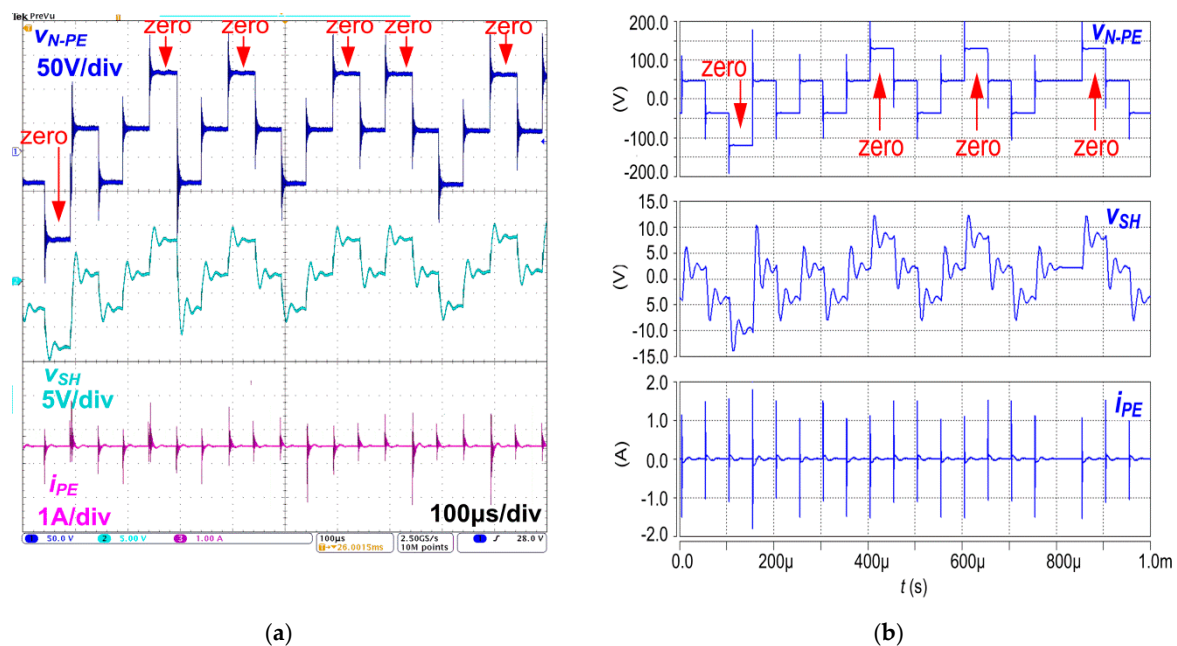

Figure 18. Waveforms of CM voltage $u_{\text{N-PE}}$, shaft voltage u_{SH}, and leakage ground current i_{PE} in a drive system fed by a hard-switched inverter: (**a**) measurement; (**b**) simulation.

It should be noted that the maximum values of voltage $v_{\text{N-PE}}$ are significantly higher than recognized for PQRDCLI. It means that maximum levels of shaft voltages in a system fed by a hard-switched inverter are also higher. Hence the probability of EDM bearings currents occurrence is higher. It should also be noted that $dv_{\text{N-PE}}/dt$ gradients are also higher than those for PQRDCLI. Thus, amplitudes of leakage currents current i_{PE} are also increased.

Additionally, a simulation of a drive system fed by a hard- switched inverter with a 720 μH common-mode choke included between machine and inverter was performed. Despite the significant reduction of i_{PE} current amplitude, levels of voltages v_S and v_{N-PE} at steady states were not limited (Figure 19). However, at transient states, a small reduction of overvoltage spikes in v_{N-PE} waveform was noticed. Simulated results are confirmed by the results of measurements, which proves the suitability of the presented modeling approach in the evaluation of CM disturbances reduction methods.
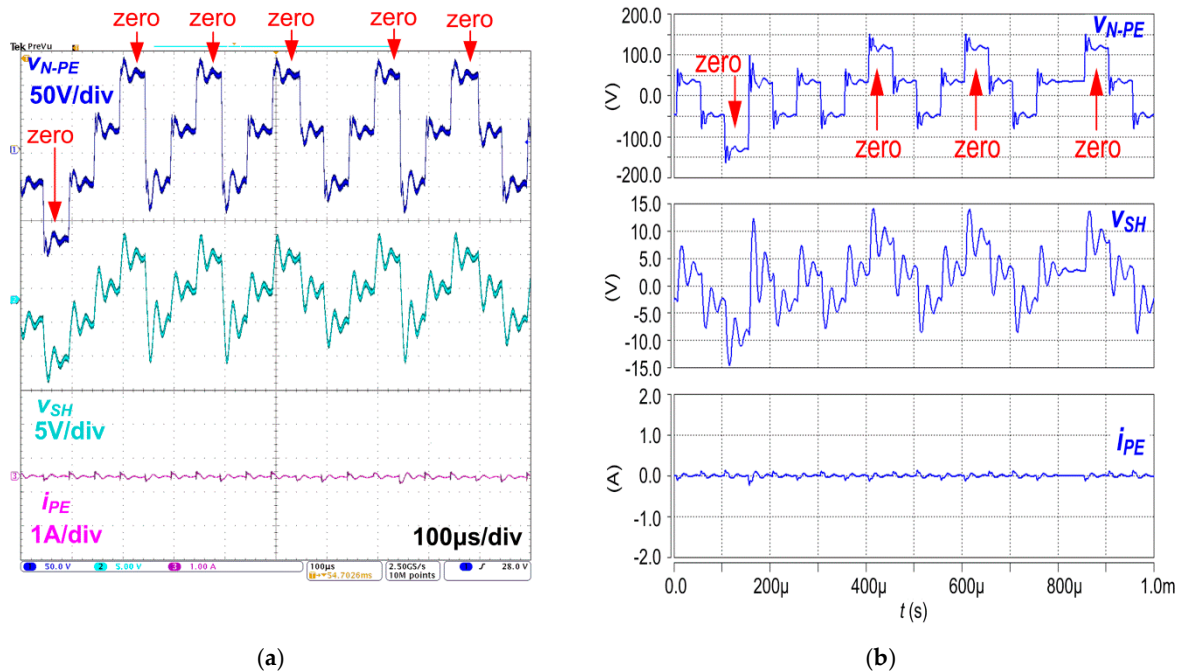

(**a**)   (**b**)

Figure 19. Waveforms of CM voltage u_{N-PE}, shaft voltage $u_{SH,}$ and leakage ground current i_{PE} in a drive system fed by a hard-switched inverter with 720 μH common-mode choke: (**a**) measurement; (**b**) simulation.

Simulation and experimental results prove that compared to the hard-switched inverter, using PQRDCLI enables a significant reduction of CM voltage amplitudes. Hence shaft voltage levels are also limited, which leads to a decrease of EDM bearing's current occurrence probability. Due to the reduction of common-mode voltage dv/dt gradients, amplitudes of bearing's currents and ground current i_{PE} resulting from dv_{N-PE}/dt are also limited. Moreover, semiconductors devices in PQRDCLI operate under lower dynamic stresses due to reduced dv/dt and di/dt gradients. Taking these aspects into account, it can be supposed that the reliability of the drive system fed by PQRDCLI should be higher than obtained for a conventional solution with a hard-switched inverter. However, this conclusion must be confirmed by the results of further research.

Relationship between efficiency and load ratio (load ratio is defined as inverter output power related to the nominal output power) of compared inverters is presented in Figure 20. At nominal output power operation, efficiency of PQRDCLI is about 0.5% higher compared to a hard-switched inverter. However, if load ratio is lower than 0.6, additional losses generated in the PQRDCLI quasi-resonant circuit are higher than switching losses in hard switching conditions. This results in lower PQRDCLI efficiency. In effect, Euro efficiency (calculated as it is presented in Ref. [33]) of PQRDCLI (93.9%) is slightly lower than obtained for compared hard-switched inverter (94.7%). Nevertheless, considering electric motors operational features, recommended operational load range should not be lower than 50% of full-load [34,35]. Hence, taking this aspect into account, PQRDCLI may be an attractive alternative for hard-switched inverters, despite of worse efficiency at light loads. An efficiency analysis proves that loss generated by PQRDCLI quasi-resonant circuit are mainly

dominated by conduction losses of transistors T_1, T_4 [8]. Therefore, further research focused on design and optimization of resonant circuit components is still required.
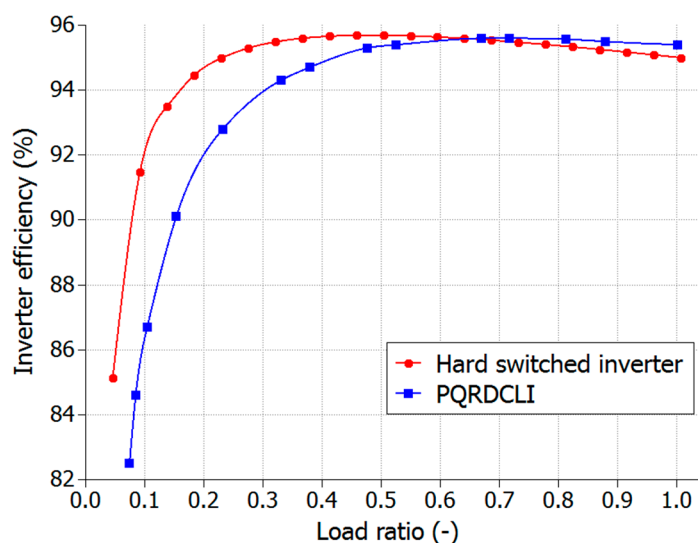

Figure 20. Measured relationship between efficiency and load ratio of hard-switched inverter and PQRDCLI.

4. Comparison with Other Solutions

The presented modeling approach was also compared with other solutions. Five hundred PQRDCLI operation periods using different models of paths, cable, and induction machines were simulated under the same simulation conditions, and the results are presented in Table 4. Tests were performed using Dell Vostro 3560 computer equipped with Intel(R) Core(TM) i7-3632QM CPU 2.20 GHz processor and 8.00 GB RAM. In the first case, models of inverter paths divided into four branches for track and based on Wheeler/Schneider formulas [12,16] were selected as a comparative solution. It should be noted that such an approach introduces a large numerical load of simulator solver, which results in a significant increase in the execution time of the simulation.

Table 4. Total execution time of simulation for individual models.

Model	Execution Time
Proposed solution	142 s
Model of the drive system with inverter model based on Wheeler/Schneider formulas paths model	430 s
Model of the drive system with an IM model presented in Ref. [14]	172 s
Model of the drive system with a cable model presented in Ref. [12]	144 s

Moreover, a large number of model parameters must be then identified, using complicated methods of parameter extraction, which additionally increases the total time of model development. The presented solution, despite using simplified models of paths (with two parameters describing each path), the accuracy of results is satisfactory with lower numerical complexity. Replacing the proposed model of IM, by solution presented in Ref. [14], results in a slight extension of the total execution time of the simulation. However, it should be noted that the model presented in Ref. [14] is described by more parameters (14 in the proposed solution, 18 in the model [14]). Moreover, the accuracy of the model [14] is lower due to the omission of IM common-mode impedance characteristic changes in-band "e" (Figure 7). It should also be noted that proposals of this paper consider the model of IM with less complicated complexity due elimination of magnetic couplings models (those are implemented in the model [14]). Replacing the described model of the cable by a model shown in Ref. [12] does not result in numerical complexity increase. A similar number of parameters also defines both models.

However, due to the elimination of phase—to—phase capacitors applied in the model [12], a procedure of parameter extraction for the proposed model became less time-consuming. It should be mentioned that the total "cost" of the model is composed of introduced numerical loads, availability of parameters, and the total time required to identify all model parameters. Hence, taking these factors into account, the modeling approach presented in this paper offers a satisfactory accuracy with a moderate "cost" of used models.

5. Conclusions

The presented modeling approach with simplified models may be successfully applied in electric drive systems simulation in a range of frequency up to 1 MHz. The procedure of the model´s parameter extraction is easy and it is based on the presented analysis of individual frequency characteristic measurements. Second, it is proposed to use available optimization algorithms. Described models of cable and induction machines may be effectively implemented in the simulation of AC drives fed by other types of inverters, e.g., multilevel DC/AC inverter. Obtained accuracy enables using the proposed modeling approach as an useful tool dedicated to the evaluation of CM disturbances reduction methods. Additionally, usefulness of PQRDCLI in CM voltage and ground leakage current reduction in electric drives was confirmed.

Conflicts of Interest: The authors declare no conflict of interest.

References

1. Shirabe, K.; Swamy, M.M.; Kang, J.K.; Hisatsune, M.; Wu, Y.; Kebort, D.; Honea, J. Efficiency Comparison Between Si-IGBT-Based Drive and GaN-Based Drive. *IEEE Trans. Ind. Appl.* **2013**, *50*, 566–572. [CrossRef]
2. Luszcz, J. *High Frequency Conducted Emission in AC Motor Drives Fed by Frequency Converters: Sources and Propagation Paths*; IEEE Press: Piscataway, NJ, USA; John Wiley & Sons: Hoboken, NJ, USA, 2018.
3. Shen, W.; Wang, F.; Boroyevich, D.; Liu, Y. Definition and acquisition of CM and DM EMI noise for general-purpose adjustable speed motor drives. In Proceedings of the 2004 IEEE 35th Annual Power Electronics Specialists Conference (IEEE Cat. No.04CH37551), Aachen, Germany, 20–25 June 2004; pp. 1028–1033. [CrossRef]
4. Muetze, A.; Binder, A. Don't lose your bearings. *IEEE Ind. Appl. Mag.* **2006**, *12*, 22–31. [CrossRef]
5. Mechlinski, M.; Schroder, S.; Shen, J.; de Doncker, R.W. Grounding Concept and Common-Mode Filter Design Methodology for Transformerless MV Drives to Prevent Bearing Current Issues. *IEEE Trans. Ind. Appl.* **2017**, *53*, 5393–5404. [CrossRef]
6. Plazenet, T.; Boileau, T.; Caironi, C.; Nahid-Mobarakeh, B. A Comprehensive Study on Shaft Voltages and Bearing Currents in Rotating Machines. *IEEE Trans. Ind. Appl.* **2018**, *54*, 3749–3759. [CrossRef]
7. Chen, S.; Lipo, T.A.; Novotny, D.W. Circulating type motor bearing current in inverter drives. In Proceedings of the IAS '96. Conference Record of the 1996 IEEE Industry Applications Conference Thirty-First IAS Annual Meeting, San Diego, CA, USA, 6–10 October 1996; Volume 1, pp. 162–167. [CrossRef]
8. Turzynski, M.; Chrzan, P.J. Reducing Common-Mode Voltage and Bearing Currents in Quasi-Resonant DC-Link Inverter. *IEEE Trans. Power Electron.* **2020**, *35*, 9555–9564. [CrossRef]
9. Akagi, H.; Tamura, S. A Passive EMI Filter for Eliminating Both Bearing Current and Ground Leakage Current from an Inverter-Driven Motor. *IEEE Trans. Power Electron.* **2006**, *21*, 1459–1469. [CrossRef]

10. Lai, Y.-S.; Chen, P.-S.; Lee, H.-K.; Chou, J. Optimal Common-Mode Voltage Reduction PWM Technique for Inverter Control with Consideration of the Dead-Time Effects—Part II: Applications to IM Drives with Diode Front End. *IEEE Trans. Ind. Appl.* **2004**, *40*, 1613–1620. [CrossRef]

11. Baranwal, R.; Basu, K.; Mohan, N. Carrier-Based Implementation of SVPWM for Dual Two-Level VSI and Dual Matrix Converter with Zero Common-Mode Voltage. *IEEE Trans. Power Electron.* **2015**, *30*, 1471–1487. [CrossRef]

12. Musznicki, P.; Turzynski, M.; Chrzan, P.J. Accurate modeling of quasi-resonant inverter fed IM drive. In Proceedings of the IECON 2013—39th Annual Conference of the IEEE Industrial Electronics Society, Vienna, Austria, 10–13 November 2013; pp. 376–381. [CrossRef]

13. Duan, Z.; Fan, T.; Wen, X.; Zhang, D. Improved SiC Power MOSFET Model Considering Nonlinear Junction Capacitances. *IEEE Trans. Power Electron.* **2018**, *33*, 2509–2517. [CrossRef]

14. Grandi, G.; Casadei, D.; Reggiani, U. Common- and Differential-Mode HF Current Components in AC Motors Supplied by Voltage Source Inverters. *IEEE Trans. Power Electron.* **2004**, *19*, 16–24. [CrossRef]

15. Revol, B.; Roudet, J.; Schanen, J.-L.; Loizelet, P. EMI Study of Three-Phase Inverter-Fed Motor Drives. *IEEE Trans. Ind. Appl.* **2011**, *47*, 223–231. [CrossRef]

16. Bogatin, E. Design rules for microstrip capacitance. *IEEE Trans. Compon. Hybrids Manuf. Technol.* **1988**, *11*, 253–259. [CrossRef]

17. Lai, J.S.; Huang, X.; Pepa, E.; Chen, S.; Nehl, T.W. Inverter EMI modeling and simulation methodologies. *IEEE Trans. Ind. Electron.* **2006**, *53*, 736–744. [CrossRef]

18. Yuan, L.; Yu, H.; Wang, X.; Zhao, Z. Design, simulation and analysis of the low stray inductance bus bar for voltage source inverters. In Proceedings of the 2011 International Conference on Electrical Machines and Systems, Beijing, China, 20–23 August 2011; pp. 1–5. [CrossRef]

19. Kedarisetti, J.; Mutschler, P. A Motor-Friendly Quasi-Resonant DC-Link Inverter with Lossless Variable Zero-Voltage Duration. *IEEE Trans. Power Electron.* **2012**, *27*, 2613–2622. [CrossRef]

20. Smith, L.D.; Hockanson, D. Distributed SPICE circuit model for ceramic capacitors. In Proceedings of the 51st Electronic Components and Technology Conference (Cat. No.01CH37220), Orlando, FL, USA, 29 May–1 June 2001; pp. 523–528. [CrossRef]

21. Wijenayake, A.H.; Braun, D.H.; Gasperi, M.L.; Gilmore, T.P.; Pixler, D.C. Modeling and analysis of DC link bus capacitor and inductor heating effect on AC drives. In Proceedings of the IAS '97 Conference Record of the 1997 IEEE Industry Applications Conference Thirty-Second IAS Annual Meeting, New Orleans, LA, USA, 5–9 October 1997; Volume 2, pp. 1052–1057. [CrossRef]

22. Ardizzoni, J. A Practical Guide to High-Speed Printed-Circuit-Board Layout. *Analog Dialogue* **2005**, *39*, 1–6.

23. Turzynski, M.; Kulesza, W.J. A Simplified Behavioral MOSFET Model Based on Parameters Extraction for Circuit Simulations. *IEEE Trans. Power Electron.* **2016**, *31*, 3096–3105. [CrossRef]

24. Lauritzen, P.O.; Ma, C.L. A simple diode model with reverse recovery. *IEEE Trans. Power Electron.* **1991**, *6*, 188–191. [CrossRef]

25. Shami, U.T.; Akagi, H. Identification and Discussion of the Origin of a Shaft End-to-End Voltage in an Inverter-Driven Motor. *IEEE Trans. Power Electron.* **2010**, *25*, 1615–1625. [CrossRef]

26. Ohara, S.; Ogasawara, S.; Masatsugu, T.; Orikawa, K.; Yamamoto, Y. A novel active common-noise canceler combining feedforward and feedback control. In Proceedings of the 2017 IEEE Energy Conversion Congress and Exposition (ECCE), Cincinnati, OH, USA, 1–5 October 2017; pp. 2469–2475. [CrossRef]

27. Turzyński, M. Induction machine behavioral modeling for prediction of EMI propagation. *Bull. Pol. Acad. Sci. Tech. Sci.* **2017**, *65*, 247–254. [CrossRef]

28. Chen, S.; Lipo, T.A.; Fitzgerald, D. Source of induction motor bearing currents caused by PWM inverters. *IEEE Trans. Energy Convers.* **1996**, *11*, 25–32. [CrossRef]

29. GNU Octave: Minimizers. Available online: https://octave.org/doc/v4.0.0/Minimizers.html (accessed on 17 June 2020).

30. Nieznanski, J.; Wojewodka, A.; Chrzan, R.J. Comparison of vector sigma-delta modulation and space-vector PWM. In Proceedings of the 2000 26th Annual Conference of the IEEE Industrial Electronics Society. IECON 2000. 2000 IEEE International Conference on Industrial Electronics, Control and Instrumentation 21st Century Technologies and Industrial Opportunities (Cat. No.00CH37141), Nagoya, Japan, 22–28 October 2000; Volume 2, pp. 1322–1327. [CrossRef]

31. Weber, S.-P.; Hoene, E.; Guttowski, S.; John, W.; Reichl, H. Modeling induction machines for EMC-Analysis. In Proceedings of the 2004 IEEE 35th Annual Power Electronics Specialists Conference (IEEE Cat. No.04CH37551), Aachen, Germany, 20–25 June 2004; pp. 94–98. [CrossRef]

32. Muetze, A.; Binder, A. Calculation of Motor Capacitances for Prediction of the Voltage Across the Bearings in Machines of Inverter-Based Drive Systems. *IEEE Trans. Ind. Appl.* **2007**, *43*, 665–672. [CrossRef]

33. Pearsall, N. (Ed.) *The Performance of Photovoltaic (PV) Systems: Modelling, Measurement and Assessment*; Woodhead Publishing: Amsterdam, The Netherlands; Boston, MA, USA, 2017.

34. Determining Electric Motor Load and Efficiency. In *USA DOE Motor Challenge, A Program of the USA Department of Energy*; USA Department of Energy, Office of Energy Efficiency and Renewable Energy: Washington, DC, USA, 1997.

35. Li, Y.; Liu, M.; Lau, J.; Zhang, B. A novel method to determine the motor efficiency under variable speed operations and partial load conditions. *Appl. Energy* **2015**, *144*, 234–240. [CrossRef]